



Bulletin of the Mineral Research and Exploration

<http://bulletin.mta.gov.tr>



Modelling and computation of gravitational attraction, gradient tensors, rotational and horizontal invariants of Asteroid Bennu (101955), Itokawa (25143) and Eros (433) via 2D Non-Uniform FFT

İlkin ÖZSÖZ^{a*}

^a General Directorate of Mineral Research and Exploration, Department of Marine Research, Ankara, Türkiye

Research Article

Keywords:

2D NU-FFT, Bennu (101955), Itokawa (25143), Eros (433), Gravity gradient tensors.

ABSTRACT

The internal structure and mass distribution of the terrestrial objects are yet unknown. The 2D gravity model with a constant density of the terrestrial objects can shed light on the surficial or textural heterogeneity due to topographic variations of the terrestrial objects. Three different asteroids, which are Bennu (101955), Itokawa (25143) and Eros (433) are modelled in this study. During the modelling phase, a different number of edges, elements, nodes, and faces are used to describe the 3D models of Bennu, Itokawa, and Eros. These 3D models are used in 2D Non-Uniform Fast Fourier Transform (NU-FFT) applications to obtain gravitational attraction with a constant density polyhedron model. Tensor gradients and tensor invariants of the modelled gravity anomaly are calculated. Three major outcomes are interpreted from tensor gradient and tensor invariants. Firstly, textural heterogeneity due to relatively low topography is detected in the central part of Bennu. Secondly, considerably different properties which can be related to surface variations between the two lobes of Itokawa are observed. Lastly, directional surficial heterogeneities were detected in Eros.

Received Date: 28.04.2022

Accepted Date: 14.02.2023

1. Introduction

The forward solution of the gravity potential and its derivatives are considered to have a widespread application for different subjects. The gravity potential is described as a volume integral, and the volume integral is generally solved in the space domain by analytical methods. Alternatively, spectral-domain solutions can be used to solve volume integrals. If space domain and spectral domain solutions are compared, it is possible to say that space domain solutions are more accurate but cost more computation time. Therefore, spectral-domain solutions are the more appropriate

method for computing the gravity effect of the 2D/3D grids with small grid spacing.

Cooley and Tukey (1965) fundamentally described the FFT algorithm. In this study, FFT process was applied in three steps. Firstly, the Fourier transform of the given 2D/3D grid is computed. Then, the data is analytically or numerically solved in the spectral domain. Lastly, the spectrum is transformed back to the space domain by the inverse Fourier transform. Analytical solutions of the gravity effect in the spectral domain for the rectangular prism with constant and variable density are derived by many authors

Citation Info: Önsöz, İ. 2024. Modelling and computation of gravitational attraction, gradient tensors, rotational and horizontal invariants of Asteroid Bennu (101955), Itokawa (25143) and Eros (433) via 2D Non-Uniform FFT. Bulletin of the Mineral Research and Exploration 173, 1-18. <https://doi.org/10.19111/bulletinofmre.1251299>

*Corresponding author: İlkin ÖZSÖZ, ilkin.ozsoz@mta.gov.tr

(Bhattacharyya, 1966; Chai and Hinze, 1988; Chenot and Debeglia, 1990; Lee and Biehler, 1991; Tontini et al., 2009; Wu and Chen, 2016). Furthermore, these analytical solutions of the gravity effect can be derived using polyhedron models with constant or variable density (Pedersen, 1978; Wu, 1983; Hansen and Wang, 1988).

The gravity vector and its gradient tensor can be expressed by differential relation in the spectral-domain (Wu, 2019). Wu and Chen (2016) mentioned the major limitations of the Fourier transform are quadrature error and truncation error within the computed forward anomaly. In order to eliminate major drawbacks of Fourier-domain methods, the non-uniform FFT (NU-FFT) technique was introduced by Wu and Tian (2014) and Wu (2021). This technique uses both the shift sampling method (Chai and Hinze, 1988) and Gauss quadrature rules. Many authors (Wu and Tian, 2014; Wu, 2016; Wu and Chen, 2016; Wu and Lin, 2017; Wu, 2019; Wu, 2021a) showed that the NU-FFT algorithm produces better results than the conventional FFT algorithm for arbitrary-shaped models. Furthermore, less quadrature error was observed in NU-FFT results than in conventional FFT. However, neither NUFFT nor traditional FFT methods can eliminate truncation errors, which are controlled by Nyquist frequency.

NU-FFT and gradient tensor applications in the spectral domain were applied to Bennu, Itokawa, and Eros asteroids. The noticeable properties of Bennu, Itokawa and Eros can be summarised as; (1) weathering, impact, and other processes have altered the surface of Bennu, as evidenced by mass displacement, cracks, and craters (Barnouin et al., 2019; DellaGiustina et al., 2019; Walsh et al., 2019), (2) Itokawa appears to be composed of a rubble-pile structure rather than a single integrated mass (Saito et al., 2006), (3) Eros has a cratered surface and is also encrusted in a layer of regolith and rocks (Veverka et al., 2001; Chapman et al., 2002; Robinson et al., 2002; Thomas et al., 2002; Richardson et al., 2004).

The aim of this paper is to digitize 3D models of Itokawa, Eros and Bennu asteroids and compute their gravity anomalies and gradient tensors by the 2D NU-FFT technique. The modelled gradient tensors are

used in the computation of rotational and horizontal invariants which can be used as edge detection techniques, surficial heterogeneity analysis due to abnormal elevation or topography for the asteroid models. The paper offers that digitising various file extensions (“.off”, “.stl”, “.ply” and “.mesh”) to obtain elements, faces and edges of the provided 3D model and compute its gravity anomaly and gradients for rotational and horizontal invariant techniques to detect major surficial heterogeneities of the celestial bodies. Briefly, the results of this study indicate that an anomalous forward modelled gravity anomaly due to relatively low topography is discovered in the middle region of Bennu, significant differences in surficial properties are seen between Itokawa’s two lobes and directional surficial heterogeneities were discovered in Eros. The gravity field of planetary bodies could identify information about interior mass distribution if direct gravity observations were available (Scheeres et al., 2020). However, forward modelled gravity fields with constant density can only clarify the surficial or textural heterogeneities of terrestrial bodies. Since the constant density forward modelling algorithm was used, the inner structure of the asteroid could not be interpreted. The lows and highs in gravity anomaly and its derivatives can be linked to topographical variations.

2. Physical Properties of Asteroid Bennu, Itokawa and Eros

2.1. Asteroid Bennu (101955)

The asteroid was discovered on 11 September 1999 by the Lincoln Near-Earth Asteroid Research program (Stokes et al., 2000). Bennu (101955) is a small near-Earth celestial body with a half kilometer diameter and an equatorial bulge (Figure 1). The structure of the asteroid Bennu is a rubble-pile, which is inferred from low-density measurements, and its surface is rocky (Barnouin et al., 2019; DellaGiustina et al., 2019; Lauretta et al., 2019; Scheeres et al., 2019; McMahan et al., 2020). Scheeres et al., (2019) suggested that the dynamical evolution of Bennu is quite complex owing to the non-spherical shape of its body.

The surface of Bennu is affected by weathering, impact, and other processes since mass movement, fractures, and craters are noted (Barnouin et al., 2019;

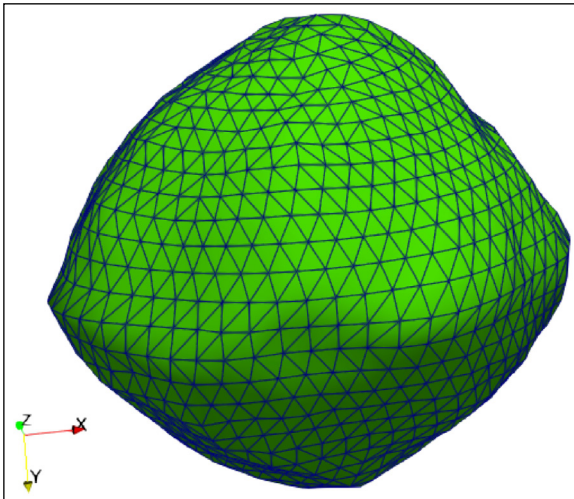


Figure 1- Shape of the asteroid Bennu with digitised edges.

DellaGiustina et al., 2019; Walsh et al., 2019). Signs of exfoliation events are observed in the boulders of Bennu due to the existence of disaggregated thin layers at the surface (Molaro et al., 2020a). According to Molaro et al., (2020b), physical features of an asteroid Bennu stems from the thermal fatigue process, which might be linked to thermal cycling (Holzhausen, 1989).

Asteroid Bennu was modelled (Molaro et al., 2015; Hazeli et al., 2018; El Mir et al., 2019) and laboratory studies (Thirumalai and Demou, 1970; Levi, 1973; Delbo et al., 2014) were conducted in terms of the thermal fatigue process by many researchers. The results of models and laboratory work suggested that chemical and biogenic weathering due to thermal fatigue triggered the exfoliation of rock boulders (Waragai, 1998; McFadden et al., 2005; Fletcher et al., 2006; Eppes et al., 2010; Eppes and Keanini, 2017; Lamp et al., 2017).

Chesley et al. (2014) investigated the bulk density of Bennu via orbital deviations and thermal missions. The estimated bulk density of asteroid Bennu is

$1260 \pm 70 \text{ kg/m}^3$. Furthermore, they shed light on the rubble-pile internal structure of Bennu by presenting the macro-porosity range as $40 \pm 10 \%$. The mass of the terrestrial body is estimated as $7.8 \pm 0.9 * 10^{10} \text{ kg}$ and $GM = 5.2 \pm 0.6 \text{ m}^3/\text{s}^2$ (Chesley et al., 2014). The size and shape parameters of Bennu are provided in Table 1.

2.2. Asteroid Itokawa (25143)

The asteroid was discovered on 26 September 1998 by the Lincoln Near-Earth Asteroid Research program (Stokes et al., 2000). In November 2005, the Hayabusa spacecraft collected regolith samples on the asteroid's surface, and these samples returned to Earth in June 2010 (Yano et al., 2006; Tanbakouei et al., 2019). Nakamura et al. (2011) showed that vast rocks and stones are non-uniformly distributed on Itokawa's surface. Itokawa seems likely to have a rubble-pile structure instead of a single consolidated structure. A wide range of boulder sizes, ranging from meters to hundreds of meters, are analysed on the surface of Itokawa (Saito et al., 2006).

Fujiwara et al. (2006) resembled Itokawa's shape to a sea otter (Figure 2). The asteroid consisted of a smaller head part and a larger body part. The head part of Itokawa has more facets (Saito et al., 2006) rather than the body part and this physical characteristic has been taken into account during the modelling stage. The body and head parts have a rounded shape which indicates a long period of evolution (Fujiwara et al., 2006).

Whiteley et al. (2002) claimed that Itokawa might be either a loosely consolidated body or a young terrestrial body that has been exposed to collisional disruption. Large facets on Itokawa indicate that the asteroid has experienced large impacts in the past, but these impacts cannot be transmitted to the internal

Table 1- Bennu size and shape parameters (Lauretta et al., 2015)

Parameter	Value	Uncertainty (\pm)
Mean diameter (m)	492	20
Polar dimension (m)	508	52
Equatorial dimensions (m)	565 x 535	10
Volume (km^3)	0.0623	0.006
Surface Area (km^2)	0.786	0.04

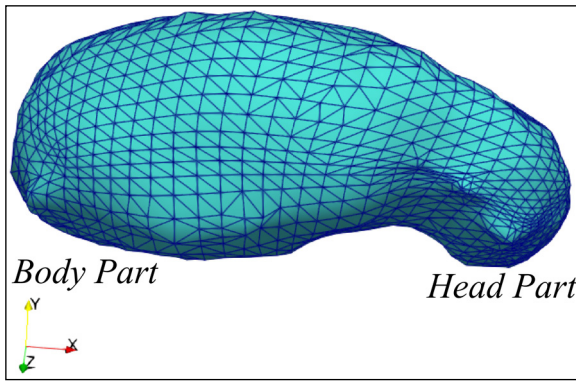


Figure 2- Shape of the asteroid Itokawa with digitised edges.

body due to the high porosity structure (Asphaug et al., 1998).

There are two scenarios for the origin of Itokawa. The first scenario suggests that the head part and body part were formed separately (Saito et al., 2006). Then, these two parts contacted at a relatively slow speed, and the original shape of the body and head parts was protected (Saito et al., 2006). The second scenario suggests that a large impact formed the neck part, which is located between the head and body parts (Fujiwara et al., 1993). Before the impact event, the asteroid was a single body (Fujiwara et al., 1993).

The physical properties of asteroid Itokawa were found by the Hayabusa spacecraft. These properties are provided in Table 2.

2.3. Asteroid Eros (433)

Asteroid Eros was discovered on 13 August 1989 by Gustav Witt (Yeomans, 1995) and it was observed before any definition between 30 November 1988 and 5 December 1988 with the Arecibo telescope (Ostro et al., 1992; Magri et al., 2001). Near-Earth Asteroid Rendezvous (NEAR) mission (Cheng et al., 1997) provided crucial information about Eros' pole orientation, spin rate, orbit, mineralogy, chemical

composition and internal structure (McCoy et al., 2000). The mission was started on 14 February 2000. The results of the mission indicated that Eros has a cratered surface and covered with a regolith layer and boulders (Veveřka et al., 2001; Chapman et al., 2002; Robinson et al., 2002; Thomas et al., 2002; Richardson et al., 2004).

Eros is an S-class asteroid (Figure 3) that is composed of pyroxene, olivine, plagioclase, and ordinary chondrites (McCoy et al., 2000). There are two theories about the formation of the asteroid Eros. The first theory claims that space weathering and differentiation processes result in hemispheric-scale heterogeneity (Murchie and Pieters, 1996; Veverka et al., 1999). The other theory states that the existence of ordinary chondrites presents unaltered composition from the solar system's formation process. The chemical structure of ordinary chondrites is almost identical to that of the Sun. Therefore, it might be said that Eros is an unaltered body after the accretion of the chondrites (Yeomans, 1995).

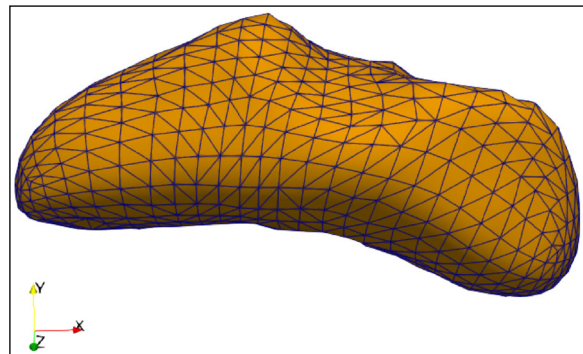


Figure 3- Shape of the asteroid Eros with digitised edges.

The Near mission provided the size and shape parameters of Asteroid Eros. These parameters of the Asteroid Eros are illustrated in Table 3.

Table 2- Itokawa size and shape parameters (Fujiwara et al., 2006).

Parameter	Value	Uncertainty (\pm)
Size (m)	535 x 294 x 209	1
Density (kg/cm ³)	1000	130
Mass (kg)	3.51 x 10 ¹⁰	0.105 x 10 ¹⁰
Volume (m ³)	1.84 x 10 ⁷	0.092 x 10 ⁷

Table 3- Eros size and shape parameters (Miller et al., 2002; Konopliv et al., 2002; Kanamaru et al., 2019).

Parameter	Value	Uncertainty (\pm)
Size (km)	13 x 13 x 33	–
Density (kg/cm ³)	2670	30
Mass (kg)	6.6904 x 10 ¹⁵	0.003 x 10 ¹⁵
Volume (km ³)	2503	25

3. Methods

3.1. Digitizing and Re-Modelling of 3D Asteroid Models

3D models of the asteroids were downloaded from <https://solarsystem.nasa.gov/>. The models can be downloaded as either gITF or USDZ file. In this paper, gITF file (.glb) format is used for Bennu, Itokawa and Eros models.

The “gITF” file format can be visualised in ParaView which is open-source data analysis and visualisation software. Paraview’s Visualisation Toolkit comprises C++, Java and Python libraries to process the input model and visualise the processed model. For a large dataset, ParaView can use distributed memory to shorten the processing time. Furthermore, ParaView allows users to convert file formats from “.glb” to “.stl” (Ayachit et al., 2015). In this study, the “.stl” file format is required to digitise edges, elements (or mesh tetrahedral), faces, and nodes (or mesh points) of the given 3D model. Therefore, Paraview was used for the conversion of data formats to “.stl” and for visualising the converted 3D model (Table 4).

After conversion from “.glb” to “.stl”, data is ready for the digitising phase. Tetgen open-source C++ program can be used for digitising processes for arbitrary complex models. It can generate tetrahedral meshes to detect edges, elements, faces, and nodes of the given model. Various file extensions (.off, .stl, .ply and .mesh) are readable in Tetgen (Si, 2015). In this study, the “.stl” format, which was converted from “.glb” in Paraview, was used as an input file extension

in Tetgen. To extract, nodes (.node), elements (.ele), faces (.face) and edges (.edge), “tetgen -fe Name.stl” command was run in Windows Powershell or Git Bash. The outputs of Tetgen were used in Matlab code for re-modelling asteroids Bennu, Itokawa and Eros.

3.2. 2D Non-Uniform FFT (NU-FFT)

The defects of standard FFT based forward solutions are the finite length and discretization effects (Wu and Tian, 2014). Wu and Tian (2014) described the finite length effect as a cut point of an infinite Fourier integral at the Nyquist frequency. Furthermore, the discretization effect stems from the finite integral’s maximum and minimum limits at the Nyquist frequency.

Finite length errors can be ignored for potential field studies due to the amplitude of the spectrum decaying exponentially with increasing wavenumber. However, the discretization effect cannot be neglected since the oscillations of the Fourier integral may be inadequately covered by the trapezoidal rule. In this case, a smaller interval for the trapezoidal rule is mandatory for the standard FFT method. In other words, grid expansion should be applied to avoid the discretization effect. The other option to minimize discretization error is using the 2D Gaussian quadrature rule. Additionally, the standard FFT forward results produce quite reliable results as long as the source lies in the centre of the window. However, if the position of the source does not lie in the centre of the window, the edge effects tend to occur. This problem can be solved by grid

Table 4- Number of digitised faces, edges, elements and nodes for each input model.

Model Name	Faces	Edges	Elements	Nodes
Bennu	9750	6895	4202	1348
Itokawa	10299	7135	4488	1325
Eros	5680	3993	2456	770

expansion in the standard FFT methods, whereas the 2D Gaussian quadrature rule can automatically solve the problem via the shift-sampling technique.

According to Barnett (1976), polyhedral bodies which include polygonal bodies, can be re-modelled by triangular surfaces. Then, the 2D Gaussian quadrature rule is applied to the modelled triangular surfaces with NU-FFT (Lee and Greengard, 2005; Greengard and Lee, 2006; Keiner et al., 2009; Wu, 2016; Barnett et al., 2019; Barnett, 2021). A combination of the Gaussian quadrature rule and NU-FFT was introduced by Wu, (2021a).

In the cartesian coordinate system, $r = (x, y, z)$ presents gravity field coordinates and $\check{r} = (\check{x}, \check{y}, \check{z})$ are the coordinates of the source body. For the wavenumber domain, (k_x, k_y) corresponds to (x, y) spatial domain coordinates on a constant level ($z = z_0$). The gravity potential U can be used to obtain gravity fields in different directions and tensor gravity components in the wavenumber domain (Wu, 2016).

$$\begin{bmatrix} g_x & g_y & g_z \\ T_{xx} & T_{yy} & T_{zz} \\ T_{xy} & T_{xz} & T_{yz} \end{bmatrix} = \mathcal{F}^{-1} \left[\begin{bmatrix} ik_x & ik_y & |k| \\ -k_x^2 & -k_y^2 & |k|^2 \\ -k_x k_y & ik_x |k| & ik_y |k| \end{bmatrix} \times \mathcal{F}(U) \right]$$

where $|k| = \sqrt{k_x^2 + k_y^2}$, g_x , g_y and g_z denotes first derivative of gravity potential U and $T_{xx}, T_{yy}, T_{zz}, T_{xy}, T_{xz}, T_{yz}$ are the second derivatives of U .

The computation of U is a somewhat complex procedure for polyhedral bodies with constant density. If a polyhedron has N_F faces, the unit normal of each face is described as $n_i = (\alpha_i, \beta_i, \gamma_i)$, where $i = 1, \dots, N_F$. Additionally, J_i denotes 2D Gaussian quadrature order applied to the i^{th} facet of the polyhedron, with $j = 1, \dots, J_i$ the index for the corresponding Gaussian nodes and weights.

Gaussian nodes and weights are represented by $\check{r}_{i,j}$ and $w_{i,j}$. The index l can be replaced by the index of Gaussian quadrature nodes and weights (i, j) (Wu, 2021a):

$$N_{MP} = \sum_{i=1}^{N_F} J_i$$

$$w_{l_{1 \leq l \leq N_{MP}}} = \{w_{1,1}, \dots, w_{1,J_1}, w_{2,1}, \dots, w_{2,J_2}, \dots, w_{N_F,1}, \dots, w_{N_F,J_{N_F}}\},$$

$$\check{r}_{l_{1 \leq l \leq N_{MP}}} = \{\check{r}_{1,1}, \dots, \check{r}_{1,J_1}, \check{r}_{2,1}, \dots, \check{r}_{2,J_2}, \dots, \check{r}_{N_F,1}, \dots, \check{r}_{N_F,J_{N_F}}\},$$

$$n_{l_{1 \leq l \leq N_{MP}}} = \{n_1, \dots, n_1, n_2, \dots, n_2, \dots, n_{N_F}, \dots, n_{N_F}\},$$

where $n_1, \dots, n_1, n_2, \dots, n_2$ and n_{N_F}, \dots, n_{N_F} are repeated by J_1, J_2 and J_{N_F} times, respectively. Hence vertical component of the gravitational vector $[g_z(r)]$ can be written as (Wu, 2021a):

$$g_z(r) = -G\rho_0 \sum_{l=1}^{N_{MP}} w_l \gamma_l \frac{1}{|r - \check{r}_l|} \text{ if } \check{n}_l = (\alpha_l, \beta_l, \gamma_l)$$

where $|r - \check{r}_l|$ is Euclidian distance between the gravity field point and the quadrature point, $G = 6.67 \times 10^{-11} \text{ m}^3 \text{ kg}^{-1} \text{ s}^{-2}$ and $\rho_0 (\text{kg}/\text{m}^3)$ constant density of the polyhedral body. For 2D approximation, the gravitational effect is calculated on a constant plane $z = z_0$. Then 2D Fourier transform is applied to both sides of equation (6) (Parker, 1973; Wu, 2021a):

$$\mathcal{F}[g_z(r_0)] = -2\pi G\rho_0 e^{i k(z_0 - z_{ref})} \sum_{n=0}^{N_T} \frac{(-1)^n}{n!} |k|^{n-1} \Theta_n$$

$$\Theta_n = \mathcal{F}_{2D}^{NU} [w_l \gamma_l (\check{z}_l - z_{ref})^n]$$

$$z_{ref} = [\min(\check{z}_i) + \max(\check{z}_i)]/2$$

where N_T is Taylor series expansion order, \check{z}_{ref} denotes reference level (Wu and Lin, 2017), \mathcal{F}_{2D}^{NU} represents 2D NU-FFT application (Greengard and Lee, 2006; Wu, 2018) and \check{z}_i is depth coordinates. Finally, the Fourier transform of the gravitational potential $\mathcal{F}(U)$ is obtained by (Wu, 2016):

$$\mathcal{F}(U) = \frac{1}{|k|} \mathcal{F}[g_z(r_0)]$$

Once $\mathcal{F}(U)$ is computed, vector components of the gravity potential U is computed by equation (1). In this study, the combination of 2D NU-FFT type 1 and 2D Gaussian quadrature rule, which was proposed by Wu, (2021), is used to compute the gravitational attraction of the terrestrial bodies.

3.3. Invariant Methods

The gradient tensors can be estimated from the total magnetic field anomaly or gravity data. The important factor is the aerial coverage of the data during the tensor estimation process (Nelson, 1988a, b; Pedersen and Rasmussen, 1990).

It is known that the gravity field varies smoothly, and the decay of the field is described by the inverse square power. Additionally, invariants of the gravity field decay as inverse fourth to the ninth power. Therefore, the gradient tensors and computed invariants provide high-resolution near-surface information (Klokočník et al., 2014). The gravity gradient tensors can be described as second derivatives of the gravitational potential, U (see equation (1)). The outside of the source masses, tensor components satisfy Laplace's equation similar to the disturbing potential (U) (Floberghagen et al., 2011).

Each gravity gradient tensor contains a different type of information about the variation of the gravity field. Specifically, T_{zz} component provides geological contact information (zero contours) while the horizontal components diagnose the shape of the source body (Murphy and Dickinson, 2009; Klokočník et al., 2014). Individually, inflection points in T_{xx} and T_{yy} represent the source edge, maximum (peak) and minimum (troughs) in T_{xz} and T_{yz} are indicators of the source edge, centre point of peaks and troughs in T_{xy} marks the centre of the mass. If there is an asymmetry in T_{xy} , it indicates a dipping body. Rotational and horizontal invariants are obtained by the combination of the gravity gradient tensors.

The reason for the computation of gradient tensors and their invariants is to monitor small-scale variations in potential field data. It should be noted that gradient tensors and invariants do not provide additional information that is not already contained in the potential field. However, they may provide different insights for the interpretation stage (Pedersen and Rasmussen, 1990).

Invariants can be grouped into 2 categories; rotational and horizontal invariants. Rotational invariants are described as (Pedersen and Rasmussen, 1990; Pawlowski, 2012; Klokočník et al., 2014):

$$I_1 = T_{xx}T_{yy} + T_{yy}T_{zz} + T_{xx}T_{zz} - T_{xy}^2 - T_{yz}^2 - T_{xz}^2$$

$$I_2 = T_{xx}(T_{yy}T_{zz} - T_{yz}^2) + T_{xy}(T_{yz}T_{xz} - T_{xy}T_{zz}) + T_{xz}(T_{xy}T_{yz} - T_{xz}T_{yy})$$

Characteristics of I_1 is similar to analytic signal, but the output is always negative. Additionally, I_2 is the measure of the 3D-ness of input.

Horizontal invariants, including total horizontal derivative (THDR) and magnitude of curvature (MC), aim to detect edges of contact. The horizontal invariants can be written as (Murphy, 2007; Murphy and Dickinson, 2009):

$$THDR = \sqrt{T_{xz}^2 + T_{yz}^2}$$

$$MC = \sqrt{(T_{yy} - T_{xx})^2 + 4T_{xy}^2}$$

Peaks in $THDR$ output clarify the edges of the source, whereas local minima in MC output detect the edge of contact. Since both $THDR$ and MC mark the edge of the input, cross-checking between the two methods provides a more reliable interpretation.

4. Findings and Discussion

In this section, estimated gravity anomalies, tensor components, and invariants of the asteroids Bennu, Itokawa, and Eros are presented. Additionally, the surficial heterogeneities in terms of the forward modelled gravity anomaly with constant density of these terrestrial objects is discussed. Each result is computed by the MATLAB code, proposed by Wu, (2021b) and a colormap of the results is generated by ColorBrewer (Cynthia, 2002).

Polyhedral models are quite convenient for estimating the gravity fields of arbitrarily-shaped objects. However, polyhedral models require two assumptions; (1) the asteroid should have a polyhedral shape, (2) the density of the polyhedral shape is constant (Werner and Scheeres, 1996; Kanamaru and Sasaki, 2019).

Typically, asteroids less than 10 km in dimension tend to have rubble pile structures (Scheeres et al., 2015). It should be re-mentioned that Asteroid Bennu has a rubble-pile structure with different sizes of boulders. Hence, the size differences would disrupt the computed gravity anomaly (Scheeres et al., 2020). The gravity anomaly of Bennu is computed by a 2D NU-FFT application. The computation parameters are discussed in Section 2.1. Figure 4 indicates the 2D and 3D input models of the asteroid Bennu and the first derivatives of gravity potential (g_x, g_y, g_z).

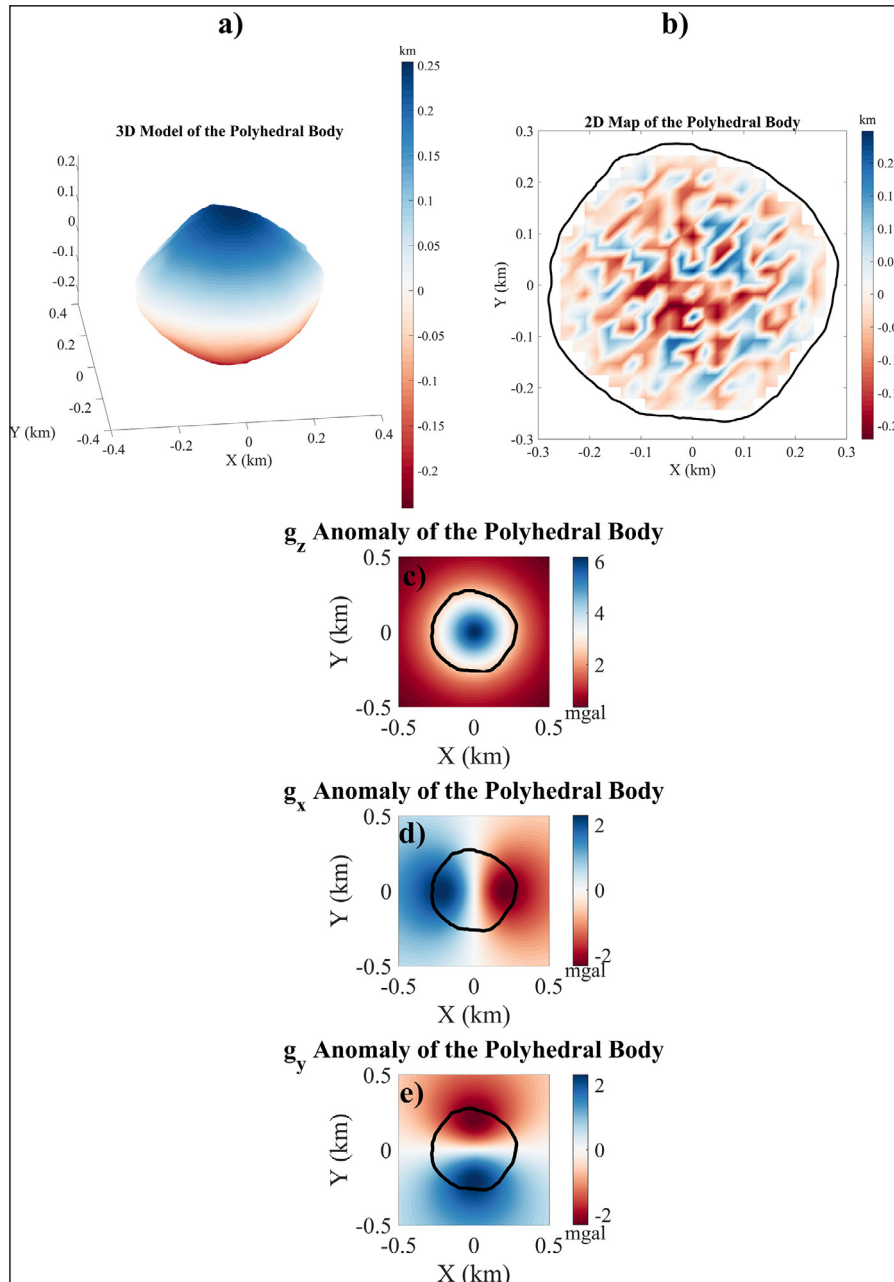


Figure 4- First derivative results for Asteroid Bennu (101955): a) 3D model of input, b) 2D model of input, c) vertical component of gravity potential U , d) X component of gravity potential U , e) Y component of gravity potential U . Solid black line delineates the boundaries of the Asteroid Bennu.

In Figure 4, the central part of the body is marked in g_x and g_y components along y and x directions, respectively. Furthermore, horizontal variations at $z=z_0$ of gravity anomaly are delineated in g_z component. Although the first derivative of gravity potential U produces interpretable results, better evaluation can be done by tensor components and invariant of the gravity field (Figure 5).

In Figure 5, the minimum estimated gravity values at the equator and centre of asteroid Bennu are compatible with previous studies (Hirabayashi and Scheeres, 2014; Sánchez and Scheeres, 2014; Lauretta et al., 2019; Scheeres et al., 2019, 2020). In the equatorial region, the material is migrating to the region where compaction is less dominant. Additionally, an equatorial bulge occurs due to the

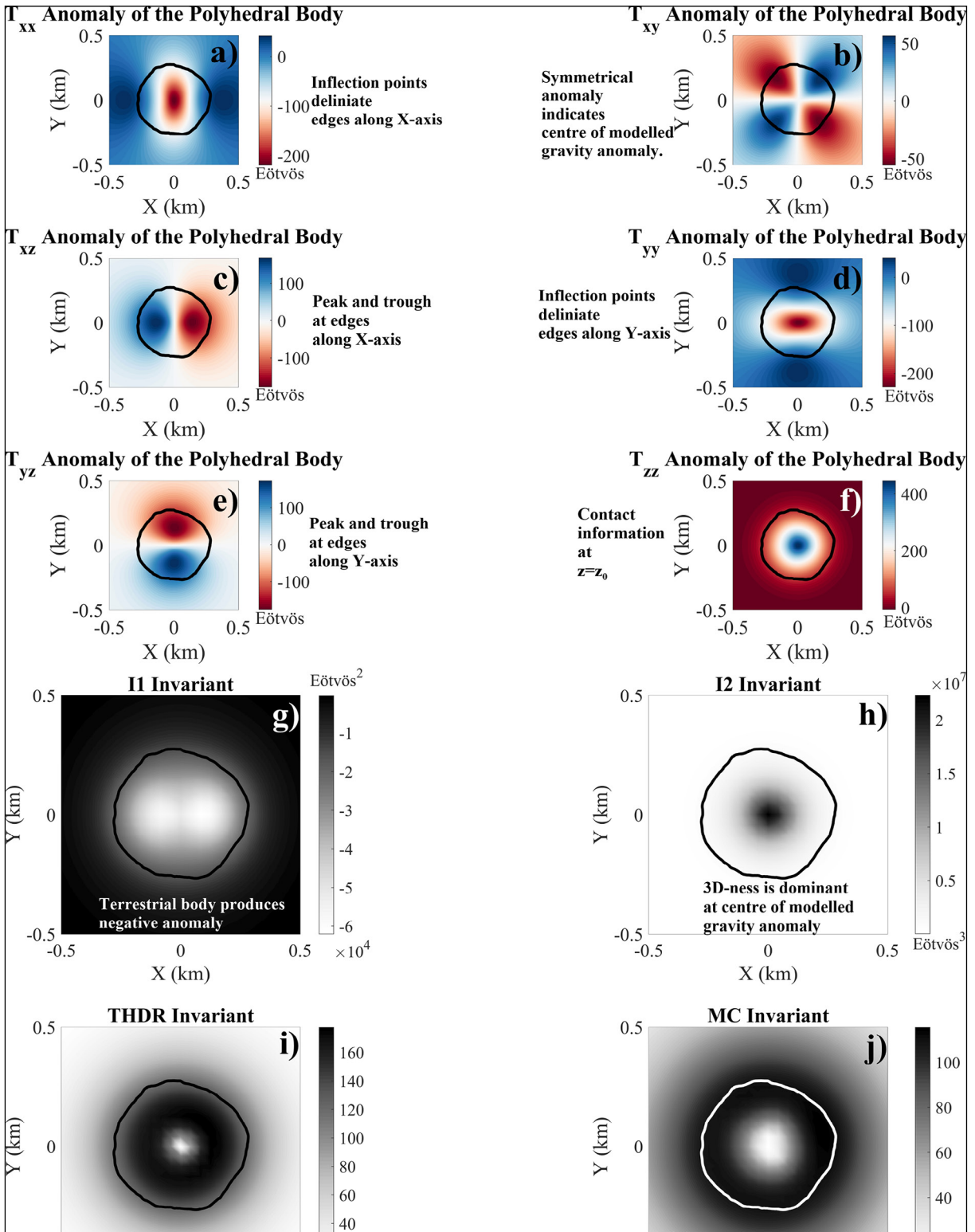


Figure 5- Second derivative results for Asteroid Bennu (101955): a) T_{xx} , b) T_{xy} , c) T_{xz} , d) T_{yy} , e) T_{yz} , f) T_{zz} , g) I_1 , h) I_2 , i) $THDR$ and j) MC .

fast spin rate of the asteroid and material migration (Hirabayashi and Scheeres, 2014; Sánchez and Scheeres, 2014).

A low gravity anomaly in the equatorial bulge of the asteroid Bennu can be associated with relatively low topography. Since the heterogeneity of this zone is quite dominant, tensors and invariants delineate its horizontal variations at $z=z_0$. Especially in g_{xy} anomaly, symmetrical peaks and troughs indicate the centre of topographic undulations with constant density. I_1 invariant provides less information about the lower topography zone, whereas I_2 , MC and $THDR$ more susceptible to variations of surficial heterogeneity.

The shape of the asteroid Bennu is more uniform than that of Itokawa. NU-FFT becomes more prominent when computing gravitational attraction of non-uniform arbitrary shapes such as Itokawa and Eros. The gravity anomaly of Itokawa is calculated via the same method that was used for the asteroid Bennu. The computation parameters are discussed in Section 2.2. Figure 6 indicates the 2D and 3D input models of Asteroid Itokawa and the first derivatives of gravity potential (g_x, g_y, g_z).

The internal structure and mass distribution of the asteroid Itokawa are yet unknown. It is known that the bulk porosity of Itokawa is approximately 40 % (Saito et al., 2006; Sánchez and Scheeres, 2014) and the mean density is roughly 1900 kg/m³ (Abe et al., 2006; Fujiwara et al., 2006).

The computed gravitational attraction results shed light on the surficial heterogeneity of Itokawa. However, the high or low density regions cannot be obtained since constant density polyhedral models are used. It is possible to say that, we assume the head and body parts of Itokawa have the same density and variations in the computed gravity anomaly should be linked to surficial heterogeneity. Sorsa et al. (2020) proposed that both lobes of Itokawa have a uniform structure and surface composition. Furthermore, the differences between lobes might be linked to void space distribution or high density metallic fragments.

The first derivative of gravity potential indicates that the body and head parts have distinct gravity

anomalies. In Figure 6c and 6d, the body part produces a distinctly higher gravity anomaly, while the head part has a lower gravity anomaly. Although the head part has higher density values (Kanamaru and Sasaki, 2019; Sorsa et al., 2020), lower gravity anomalies are estimated in g_z and g_x . It is worth noting that using constant density models during the computation of gravity anomaly does not provide a reliable density distribution. Therefore, estimated gravity anomalies cannot be associated with the density distribution of the terrestrial body. The computed gravity anomaly with constant density contrast distribution is the direct output of the surficial or textural heterogeneity. To detect variations in forward modelled gravity anomaly with constant density contrast, tensor gradient and invariant applications tend to produce more interpretable output than first derivative anomalies (Figure 7).

In Figure 7, surficial heterogeneity analysis presents anomalous characteristics in the body part, and this is compatible with the previous findings (Kanamaru and Sasaki, 2019; Sorsa et al., 2020). Tensor gradients T_{xx} and T_{yy} delineate the edge of the structural heterogeneity zone along the x and y axes. Asymmetrical anomalies in T_{xy} indicate that the position of the surficial heterogeneity is either close to the body or head part. Horizontal variations at $z=z_0$ can be tracked in T_{zz} anomaly. It is possible to say that horizontal variations forward modelled gravity anomalies with constant density contrast are observed near the body part. $THDR$ and MC outputs present extremum points where anomalous topographical variations are detected. Negative anomalies towards the body part indicate a major source of gravity anomalies in I_1 invariant. The 3D-ness of anomaly (I_2 anomaly) has a positive correlation with topographic highs and lows. The lowest values of I_2 distributed at the centre of the body whereas the highest value of I_2 is observed towards the body part. On the whole, the edge detection results indicate that there are textural heterogeneities towards the body part of the Asteroid Itokawa. Direct measurements and observations from this region may provide prominent knowledge of the nature of Itokawa.

Unlike asteroid Itokawa, Eros (433) is nearly homogeneous. Furthermore, a uniform density

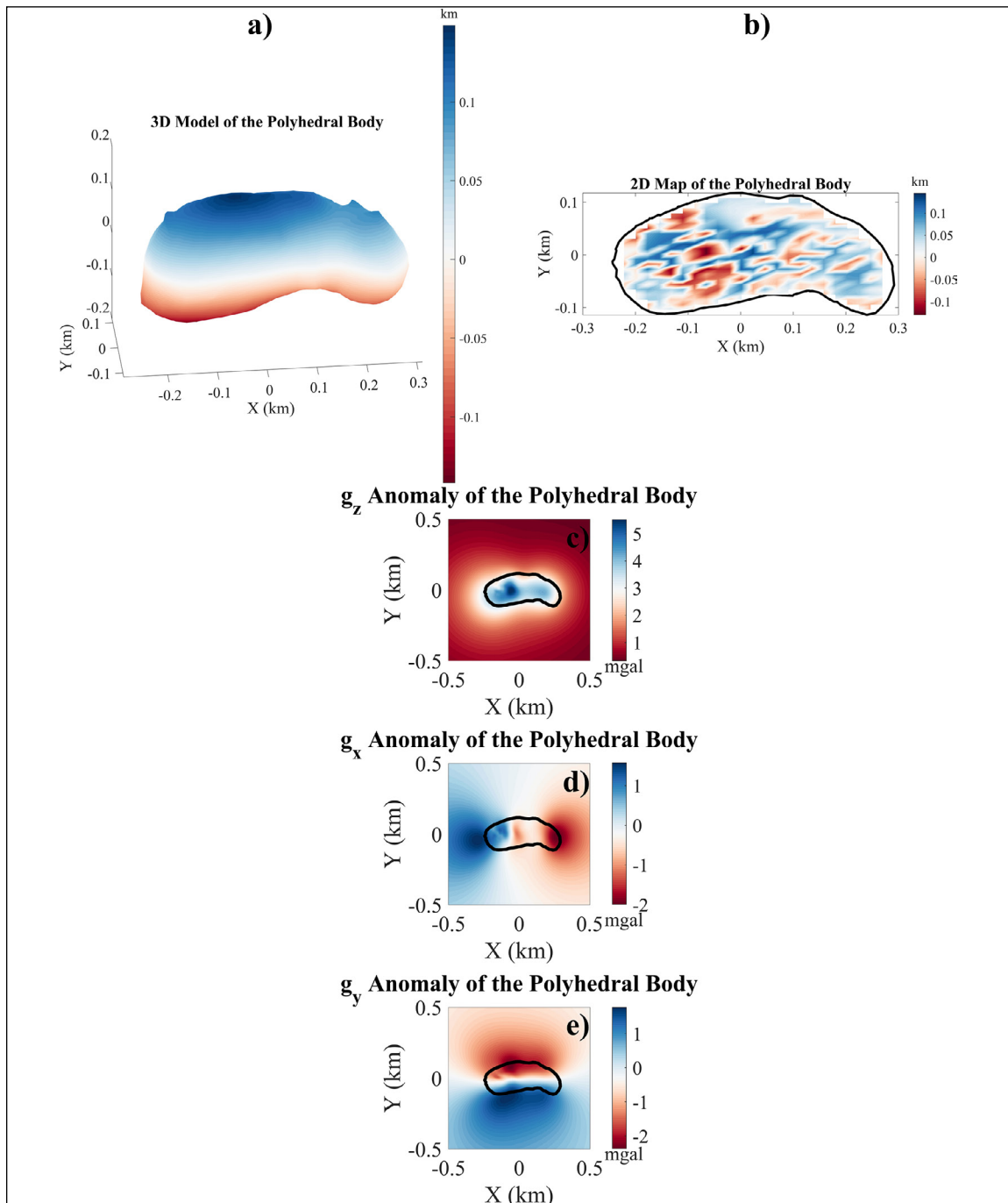


Figure 6- First derivative results for Asteroid Itokawa (25143): a) 3D model of input, b) 2D model of input, c) vertical component of gravity potential (U), d) X component of gravity potential (U), e) Y component of gravity potential (U). Solid black line delineates boundaries of the Asteroid Itokawa.

distribution is observed in the asteroid Eros (Garnier et al., 2002). Trombka et al. (2000) studied the elemental composition of Eros via the NEAR (Cheng et al. 1997) X-ray spectrometer and their findings indicated anomalous characteristics of Himeros depression (saddle-shaped structure). In order to

interpret the surficial heterogeneities of Eros and Himeros depression, the first derivatives and 2D/3D model of Asteroid Eros are illustrated in Figure 8.

Figure 8 depicts a roughly homogeneous textural heterogeneity along the X and Y axes in g_y and g_z .

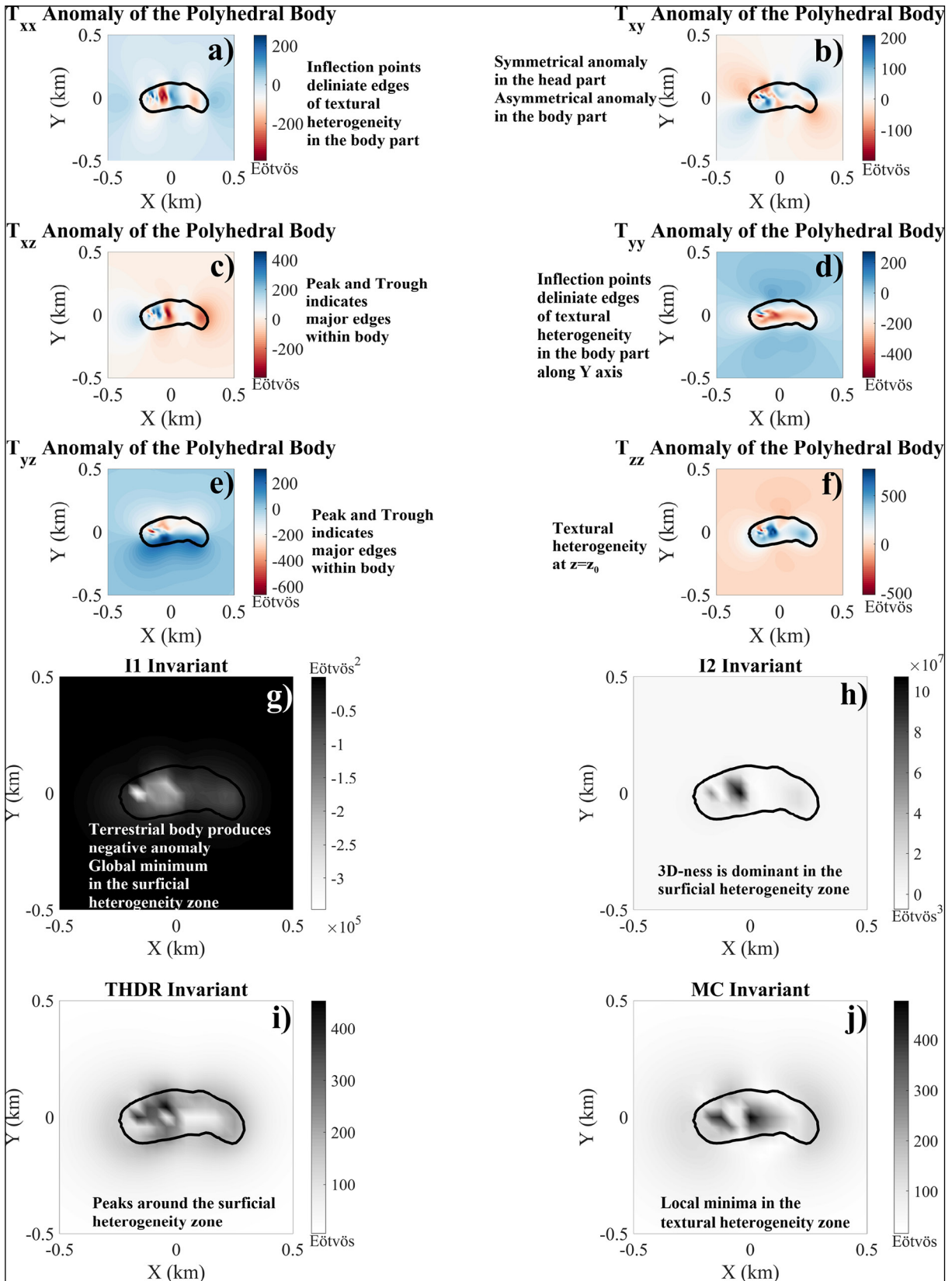


Figure 7- Second derivative results for Asteroid Itokawa (25143): a) T_{xx} , b) T_{xy} , c) T_{xz} , d) T_{yy} , e) T_{yz} , f) T_{zz} , g) I_1 , h) I_2 , i) $THDR$ and j) MC .

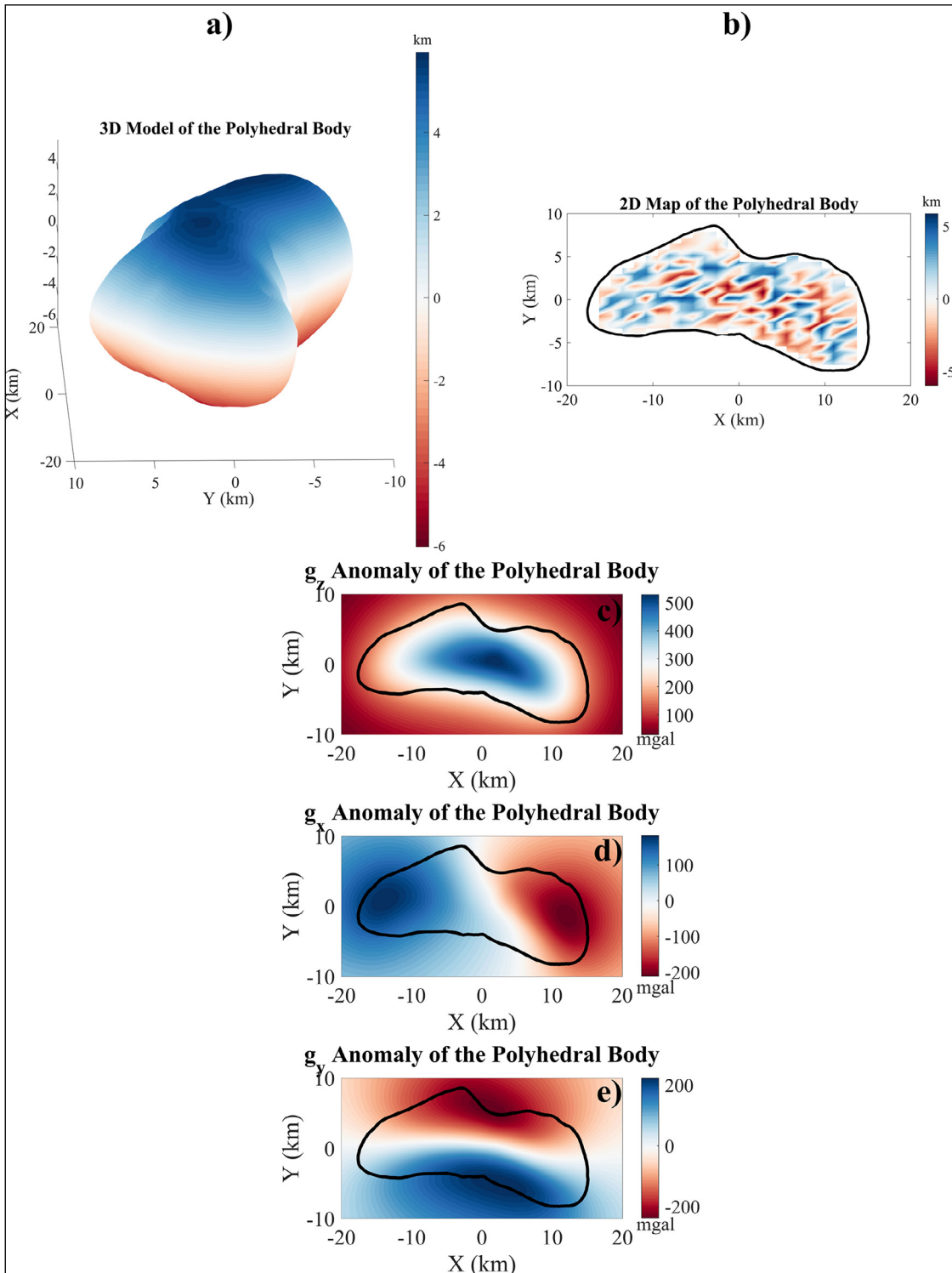


Figure 8- First derivative results for Asteroid Eros (433): a) 3D model of input, b) 2D model of input, c) vertical component of gravity potential U , d) X component of gravity potential U , e) Y component of gravity potential U . Solid black line delineates boundaries of the Asteroid Eros.

However, g_x is not symmetrical with respect to the centre of the body. This asymmetrical behaviour might be associated with heterogeneity along the

X-axis. To provide a better explanation for the surficial heterogeneity, tensors and invariants are computed (Figure 9).

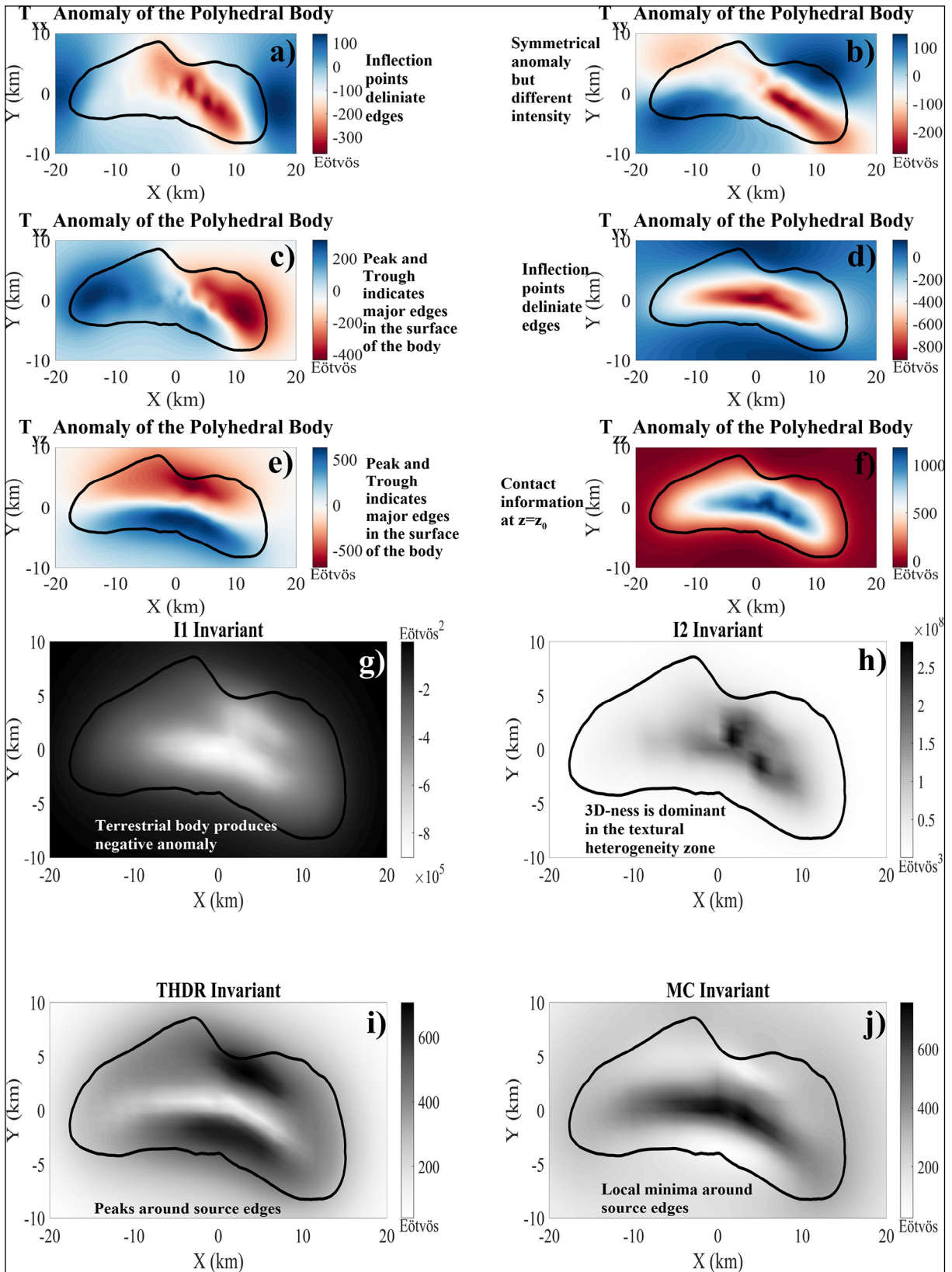


Figure 9- Second derivative results for Asteroid Eros (433): a) T_{xx} , b) T_{xy} , c) T_{xz} , d) T_{yy} , e) T_{yz} , f) T_{zz} , g) I_1 , h) I_2 , i) $THDR$ and j) MC .

For Asteroid Eros, tensors and invariants have different characteristics. For example, findings in T_{yy} indicate uniform distribution along the Y direction while T_{xx} presents heterogeneous distribution along the X-axis. This heterogeneous distribution might be linked to the saddle-shaped Himeros depression. This anomaly is compatible with the results of Trombka et al. (2000) and Garmier et al. (2002). Furthermore, T_{xz} can be used to analyse the gravity effect of Himeros depression with a roughly -100 Eötvös value. It is worth mentioning again that, although the gravity anomaly of the Himeros depression is relatively higher (Garmier et al., 2002), our study presents a lower gravity value in that region. The reason for our density models are constant and the aim is to detect surficial heterogeneities. The maximum and minimum distributions in T_{xy} are symmetrical but their intensity indicates asymmetrical behaviour around the Himeros depression.

With the exception of I_2 , the invariant methods exhibit structure-centred anomalies. However, I_2 invariant detects surficial heterogeneities in the Himeros depression, since 3D characteristics of anomaly vary in that region. I_2 invariant successfully determines the location of the heterogeneous zone. *THDR* and *MC* findings validated the nearly homogeneous structure of Eros (433) which was proposed by Garmier et al. (2002).

5. Conclusion

Information about terrestrial bodies is quite limited. Constant density forward modelling sheds light on the heterogeneities related to topographical variations. The computed gravity anomalies with constant density cannot classify high and low density regions, but they detect surficial diversity in these regions. The findings in this study were compared to previous studies for asteroids Bennu, Itokawa and Eros.

Specific characteristics of three asteroids are detected in this study. For Bennu (101955), textural heterogeneities are observed in the central part of the body. The gravity tensor and invariant of Itokawa (25143) reflect different surficial properties of the head and body parts. Finally, directional differences are detected for the asteroid Eros (433). Along the Y direction, surficial distribution in Eros

is nearly uniform, whereas surficial heterogeneities are interpreted along the X direction and Himeros depression.

References

- Abe, S., Mukai, T., Hirata, N., Barnouin-Jha, O. S., Cheng, A. F., Demura, H., Gaskell, R. W., Hashimoto, T., Hiraoka, K., Honda, T., Kubota, T., Matsuoka, M., Mizuno, T., Nakamura, R., Scheeres, D. J., Yoshikawa, M. 2006. Mass and local topography measurements of Itokawa by Hayabusa. *Science* 312 (5778), 1344–1347.
- Asphaug, E., Ostro, S. J., Hudson, R. S., Scheeres, D. J., Benz, W. 1998. Disruption of kilometre-sized asteroids by energetic collisions. *Nature* 393(6684), 437–440.
- Ayachit, U., Bauer, A., Geveci, B. 2015. ParaView catalyst: Enabling in situ data analysis and visualization. Proceedings of ISAV 2015: 1st International Workshop on In Situ Infrastructures for Enabling Extreme-Scale Analysis and Visualization, Held in conjunction with SC 2015: The International Conference for High Performance Computing, Networking, Storage 25–29.
- Barnett, C. T. 1976. Theoretical modeling of the magnetic and gravitational fields of an arbitrarily shaped three-dimensional body. *Geophysics* 41(6), 1353–1364.
- Barnett, A. H. 2021. Aliasing error of the $\exp(\beta_1 - z_2)$ kernel in the nonuniform fast Fourier transform. *Applied and Computational Harmonic Analysis* 51, 1–16.
- Barnett, A. H., Magland, J., Klinteberg, L. A. F. 2019. A parallel nonuniform fast fourier transform library based on an “Exponential of Semicircle” kernel. *Journal on Scientific Computing* 41(5), C479–C504.
- Barnouin, O. S., Daly, M. G., Palmer, E. E. 2019. Shape of (101955) Bennu indicative of a rubble pile with internal stiffness. *Nature Geoscience* 12 (4), 247–252.
- Bhattacharyya, B. K. 1966. Continuous spectrum of the total-magnetic-field anomaly due to a rectangular prismatic body. *Geophysics* 31 (1), 97–121.
- Chai, Y., Hinze, W. J. 1988. Gravity inversion of an interface above which the density contrast varies exponentially with depth. *Geophysics* 53 (6), 837–845.
- Chapman, C. R., Merline, W. J., Thomas, P. C., Joseph, J., Cheng, A. F., Izenberg, N. 2002. Impact history of Eros: Craters and boulders. *Icarus* 155 (1), 104–118.
- Cheng, A. F., Santo, A. G., Heeres, K. J., Landshof, J. A., Farquhar, R. W., Gold, R. E., Lee, S. C. 1997. Near-Earth Asteroid Rendezvous: Mission

- overview. *Journal of Geophysical Research: Planets* 102 (E10), 23695–23708.
- Chenot, D., Debeglia, N. 1990. Three-dimensional gravity or magnetic constrained depth inversion with lateral and vertical variation of contrast. *Geophysics* 55(3), 327–335.
- Chesley, S. R., Farnocchia, D., Nolan, M. C., Vokrouhlický, D., Chodas, P. W., Milani, A., Spoto, F., Rozitis, B., Benner, L. A. M., Bottke, W. F., Busch, M. W., Emery, J. P., Howell, E. S., Lauretta, D. S., Margot, J. L., Taylor, P. A. 2014. Orbit and bulk density of the OSIRIS-REx target Asteroid (101955) Bennu. *Icarus* 235, 5–22.
- Cooley, J. W., Tukey, J. W. 1965. An algorithm for the machine calculation of complex Fourier series. *Mathematics of Computation* 19 (90), 297.
- Cynthia, A. 2002. Brewer. Available at: <http://www.colorbrewer.org>.
- Delbo, M., Libourel, G., Wilkerson, J., Murdoch, N., Michel, P., Ramesh, K. T., Ganino, C., Verati, C., Marchi, S. 2014. Thermal fatigue as the origin of regolith on small asteroids. *Nature* 508 (7495), 233–236.
- DellaGiustina, D. N., Emery, J. P., Golish, D. R. 2019. Properties of rubble-pile asteroid (101955) Bennu from OSIRIS-REx imaging and thermal analysis. *Nature Astronomy* 3 (4), 341–351.
- El Mir, C., Ramesh, K. T., Delbo, M. 2019. The efficiency of thermal fatigue in regolith generation on small airless bodies. *Icarus* 333, 356–370.
- Eppes, M. C., Keanini, R. 2017. Mechanical weathering and rock erosion by climate-dependent subcritical cracking. *Reviews of Geophysics* 55 (2), 470–508.
- Eppes, M. C., McFadden, L. D., Wegmann, K. W., Scuderi, L. A. 2010. Cracks in desert pavement rocks: Further insights into mechanical weathering by directional insolation. *Geomorphology* 123 (1–2), 97–108.
- Fletcher, R. C., Buss, H. L., Brantley, S. L. 2006. A spheroidal weathering model coupling porewater chemistry to soil thicknesses during steady-state denudation. *Earth and Planetary Science Letters* 244 (1–2), 444–457.
- Floberghagen, R., Fehringer, M., Lamarre, D., Muzi, D., Frommknecht, B., Steiger, C., Piñeiro, J., da Costa Human Spaceflight, A. 2011. Mission design, operation and exploitation of the gravity field and steady-state ocean circulation explorer mission. *Journal of Geodesy* 85 (11), 749–758.
- Fujiwara, A., Kadono, T., Nakamura, A. 1993. Cratering experiments into curved surfaces and their implication for craters on small satellites. *Icarus* 105 (2), 345–350.
- Fujiwara, A., Kawaguchi, J., Yeomans, D. K. 2006. The rubble-pile asteroid Itokawa as observed by Hayabusa. *Science* 312 (5778), 1330–1334.
- Garmier, R., Barriot, J. P., Konopliv, A. S., Yeomans, D. K. 2002. Modeling of the Eros gravity field as an ellipsoidal harmonic expansion from the NEAR Doppler tracking data. *Geophysical Research Letters* 29 (8), 72–1.
- Greengard, L., Lee, J. Y. 2006. Accelerating the nonuniform fast Fourier transform. *Society for Industrial and Applied Mathematics* 46 (3), 443–454.
- Hansen, R. O., Wang, X. 1988. Simplified frequency-domain expressions for potential fields of arbitrary three-dimensional bodies. *Geophysics* 53 (3), 365–374.
- Hazeli, K., El Mir, C., Papanikolaou, S., Delbo, M., Ramesh, K. T. 2018. The origins of asteroidal rock disaggregation: Interplay of thermal fatigue and microstructure. *Icarus* 304, 172–182.
- Hirabayashi, M., Scheeres, D. J. 2014. Stress and failure analysis of rapidly rotating asteroid (29075) 1950 DA. *The Astrophysical Journal Letters* 798 (1), L8.
- Holzhausen, G. R. 1989. Origin of sheet structure, 1. Morphology and boundary conditions. *Engineering Geology* 27 (1–4), 225–278.
- Kanamaru, M., Sasaki, S. 2019. Estimation of interior density distribution for small bodies: The case of asteroid Itokawa. *Transactions of the Japan Society for Aeronautical and Space Sciences: Aerospace Technology Japan* 17 (3), 270–275.
- Kanamaru, M., Sasaki, S., Wiczorek, M. 2019. Density distribution of asteroid 25143 Itokawa based on smooth terrain shape. *Planetary and Space Science* 174, 32–42.
- Keiner, J., Kunis, S., Potts, D. 2009. Using NFFT 3---A software library for various nonequispaced fast Fourier transforms. *Association for Computing Machinery Transactions on Mathematical Software (TOMS)* 36 (4).
- Klokočník, J., Kostelecký, J., Kalvoda, J., Eppelbaum, L. V., Bezděk, A. 2014. Gravity disturbances, Marussi tensor, invariants and other functions of the geopotential represented by EGM 2008. *Journal of Earth Science Research* 2 (3), 88–101.
- Konopliv, A. S., Miller, J. K., Owen, W. M., Yeomans, D. K., Giorgini, J. D., Garmier, R., Barriot, J. P. 2002. A global solution for the gravity field, rotation, landmarks, and ephemeris of Eros. *Icarus* 160 (2), 289–299.
- Lamp, J. L., Marchant, D. R., Mackay, S. L., Head, J. W. 2017. Thermal stress weathering and the spalling of Antarctic rocks. *Journal of Geophysical Research: Earth Surface* 122 (1), 3–24.
- Lauretta, D. S., Bartels, A. E., Barucci, M. A. 2015. The OSIRIS-REx target asteroid (101955) Bennu: Constraints on its physical, geological, and dynamical nature from astronomical observations. *Meteoritics and Planetary Science* 50, 834–849.

- Lauretta, D. S., DellaGiustina, D. N., Bennett, C. A. 2019. The unexpected surface of asteroid (101955) Benu. *Nature* 568 (7750), 55–60.
- Lee, T., Biehler, S. 1991. Inversion modeling of gravity with prismatic mass bodies. *Geophysics* 56 (9), 1365–1376.
- Lee, J. Y., Greengard, L. 2005. The type 3 nonuniform FFT and its applications. *Journal of Computational Physics* 206 (1), 1–5.
- Levi, F. A. 1973. Thermal fatigue: a possible source of structural modifications in meteorites. *Meteoritics* 8 (3), 209–221.
- Magri, C., Consolmagno, G. J., Ostrch, S. J., Benner, L. A. M., Beeney, B. R. 2001. Radar constraints on asteroid regolith properties using 433 Eros as ground truth. *Meteoritics and Planetary Science* 36 (12), 1697–1709.
- McCoy, T. J., Nittler, L. R., Burbine, T. H., Trombka, J. I., Clark, P. E., Murphy, M. E. 2000. Anatomy of a partially differentiated asteroid: A “NEAR”-sighted view of Acapulcoites and Lodranites. *Icarus* 148 (1), 29–36.
- McFadden, L. D., Eppes, M. C., Gillespie, A. R., Hallet, B. 2005. Physical weathering in arid landscapes due to diurnal variation in the direction of solar heating. *Geological Society of America Bulletin* 117 (1–2), 161–173.
- McMahon, J. W., Scheeres, D. J., Chesley, S. R., French, A., Brack, D., Farnocchia, D., Takahashi, Y., Rozitis, B., Tricarico, P., Mazarico, E., Bierhaus, B., Emery, J. P., Hergenrother, C. W., Lauretta, D. S. 2020. Dynamical evolution of simulated particles ejected from Asteroid Benu. *Journal of Geophysical Research: Planets* 125 (8), e2019JE006229.
- Miller, J. K., Konopliv, A. S., Antreasian, P. G., Bordi, J. J., Chesley, S., Helfrich, C. E., Owen, W. M., Wang, T. C., Williams, B. G., Yeomans, D. K., Scheeres, D. J. 2002. Determination of shape, gravity, and rotational state of asteroid 433 Eros. *Icarus* 155 (1), 3–17.
- Molaro, J. L., Byrne, S., Langer, S. A. 2015. Grain-scale thermoelastic stresses and spatiotemporal temperature gradients on airless bodies, implications for rock breakdown. *Journal of Geophysical Research: Planets* 120 (2), 255–277.
- Molaro, J. L., Walsh, K. J., Jawin, E. R. 2020a. In situ evidence of thermally induced rock breakdown widespread on Benu’s surface. *Nature Communications* 11 (1), 1–11.
- Molaro, J. L., Hergenrother, C. W., Chesley, S. R., Walsh, K. J., Hanna, R. D., Haberle, C. W., Schwartz, S. R., Ballouz, R. L., Bottke, W. F., Campins, H. J., Lauretta, D. S. 2020b. Thermal fatigue as a driving mechanism for activity on Asteroid Benu. *Journal of Geophysical Research: Planets* 125 (8), e2019JE006325.
- Murchie, S. L., Pieters, C. M. 1996. Spectral properties and rotational spectral heterogeneity of 433 Eros. *Journal of Geophysical Research: Planets* 101 (E1), 2201–2214.
- Murphy, C. A. 2007. Interpreting FTG Gravity Data using Horizontal Tensor Components. *Electromagnetic, Gravity and Magnetic International Workshop 2017*, cp-166-00004.
- Murphy, C., Dickinson, J. 2009. Exploring exploration play models with ftg gravity data. *European Association of Geoscientists and Engineers*, cp-241-00020.
- Nakamura, T., Noguchi, T., Tanaka, M. 2011. Itokawa Dust Particles: A direct link between s-type asteroids and ordinary chondrites. *Science* 333 (6046), 1113.
- Nelson, J. B. 1988a. Calculation of the magnetic gradient tensor from total field gradient measurements and its application to geophysical interpretation. *Geophysics* 53 (7), 957–966.
- Nelson, J. B. 1988b. Comparison of gradient analysis techniques for linear two- dimensional magnetic sources. *Geophysics* 53(8), 1088–1095.
- Ostro, S. J., Campbell, D. B., Simpson, R. A. 1992. Europa, Ganymede, and Callisto: New radar results from Arecibo and Goldstone. *Journal of Geophysical Research* 97 (E11), 18227.
- Parker, R. L. 1973. The rapid calculation of potential anomalies. *Geophysical Journal International* 31 (4), 447–455.
- Pawlowski, B. 2012. Gravity gradiometry in resource exploration. *The Leading Edge* 17 (1), 51.
- Pedersen, L. B. 1978. Wavenumber domain expressions for potential fields from arbitrary 2-, 2½-, and 3-dimensional bodies. *Geophysics* 43 (3), 626–630.
- Pedersen, L. B., Rasmussen, T. M. 1990. The gradient tensor of potential field anomalies: some implications on data collection and data processing of maps. *Geophysics* 55 (12), 1558–1566.
- Richardson, J. E., Melosh, H. J., Greenberg, R. 2004. Impact-induced seismic activity on asteroid 433 Eros: A surface modification process. *Science* 306 (5701), 1526–1529.
- Robinson, M. S., Thomas, P. C., Veverka, J. 2002. The geology of 433 Eros. *Meteoritics and Planetary Science* 37 (12), 1651–1684.
- Saito, J., Miyamoto, H., Nakamura, R. 2006. Detailed images of Asteroid 25143 Itokawa from Hayabusa. *Science* 312 (5778), 1341.
- Sánchez, P., Scheeres, D. J. 2014. The strength of regolith and rubble pile asteroids. *Meteoritics and Planetary Science* 49 (5), 788–811.

- Scheeres, D. J., Britt, D., Carry, B., Holsapple, K. A. 2015. Asteroid interiors and morphology. *Asteroids IV*, 745–766.
- Scheeres, D. J., McMahon, J. W., French, A. S. 2019. The dynamic geophysical environment of (101955) Benu based on OSIRIS-REx measurements. *Nature Astronomy* 3 (4), 352–361.
- Scheeres, D. J., French, A. S., Tricarico, P. 2020. Heterogeneous mass distribution of the rubble-pile asteroid (101955) Benu. *Science Advances* 6 (41).
- Si, H. 2015. TetGen, a delaunay-based quality tetrahedral mesh generator. *Association for Computing Machinery Transactions on Mathematical Software* 41(2).
- Sorsa, L. I., Takala, M., Bambach, P., Deller, J., Vilenius, E., Agarwal, J., Carroll, K. A., Karatekin, Ö., Pursiainen, S. 2020. Tomographic inversion of gravity gradient field for a synthetic Itokawa model. *Icarus* 336, 113425.
- Stokes, G. H., Evans, J. B., Vighh, H. E. M., Shelly, F. C., Pearce, E. C. 2000. Lincoln Near-Earth Asteroid Program (LINEAR). *Icarus* 148 (1), 21–28.
- Tanbakouei, S., Trigo-Rodriguez, J. M., Sort, J., Michel, P., Blum, J., Nakamura, T., Williams, I. 2019. Mechanical properties of particles from the surface of asteroid 25143 Itokawa. *Astronomy and Astrophysics* 629, A119.
- Thirumalai, K., Demou, S. G. 1970. Effect of reduced pressure on thermal-expansion behavior of rocks and its significance to thermal fragmentation. *Journal of Applied Physics* 41(13), 5147–5151.
- Thomas, P. C., Joseph, J., Carcich, B. 2002. Eros: Shape, topography, and slope processes. *Icarus* 155 (1), 18–37.
- Tontini, F. C., Cocchi, L., Carmisciano, C. 2009. Rapid 3-d forward model of potential fields with application to the palinuro seamount magnetic anomaly (Southern Tyrrhenian Sea, Italy). *Journal of Geophysical Research: Solid Earth* 114 (2), 2103.
- Trombka, J. I., Squyres, S. W., Bruckner, J. 2000. The Elemental Composition of Asteroid 433 Eros: Results of the NEAR-Shoemaker X-ray Spectrometer. *Science* 289 (5487), 2101–2105.
- Veverka, J., Thomas, P. C., Bell, J. F. 1999. Imaging of Asteroid 433 Eros during NEARs Flyby Reconnaissance. *Science* 285 (5427), 562–564.
- Veverka, J., Thomas, P. C., Robinson, M. 2001. Imaging of small-scale features on 433 Eros from NEAR: Evidence for a complex regolith. *Science* 292 (5516), 484–488.
- Walsh, K. J., Jawin, E. R., Ballouz, R. L. 2019. Craters, boulders and regolith of (101955) Benu indicative of an old and dynamic surface. *Nature Geoscience* 12 (4), 242–246.
- Waragai, T. 1998. Effects of rock surface temperature on exfoliation, rock varnish, and lichens on a boulder in the Hunza Valley. *Arctic and Alpine Research* 30 (2), 184–192.
- Werner, R. A., Scheeres, D. J. 1996. Exterior gravitation of a polyhedron derived and compared with harmonic and mascon gravitation representations of asteroid 4769 Castalia. *Celestial Mechanics and Dynamical Astronomy* 65 (3), 313–344.
- Whiteley, R. J., Tholen, D. J., Hergenrother, C. W. 2002. Lightcurve Analysis of four new monolithic fast-rotating asteroids. *Icarus* 157 (1), 139–154.
- Wu, X. 1983. The computation of the spectrum of potential field due to 3-D arbitrary bodies with physical parameters varying with depth. *Acta Geophysica Sinica* 26 (2), 177–187.
- Wu, L. 2016. Efficient modelling of gravity effects due to topographic masses using the Gauss-FFT method. *Geophysical Journal International* 205 (1), 160–178.
- Wu, L. 2018. Comparison of 3-D Fourier forward algorithms for gravity modelling of prismatic bodies with polynomial density distribution. *Geophysical Journal International* 215 (3), 1865–1886.
- Wu, L. 2019. Fourier-domain modeling of gravity effects caused by polyhedral bodies. *Journal of Geodesy* 93 (5), 635–653.
- Wu, L. 2021a. Modified Parker’s method for gravitational forward and inverse modeling using general polyhedral models. *Journal of Geophysical Research: Solid Earth* 126 (10).
- Wu, L. 2021b. Data and code for “Modified Parker’s method for gravitational forward and inverse modeling using general polyhedral models”.
- Wu, L., Tian, G. 2014. High-precision fourier forward modeling of potential fields. *Geophysics* 79 (5), G59–G68.
- Wu, L., Chen, L. 2016. Fourier forward modeling of vector and tensor gravity fields due to prismatic bodies with variable density contrast. *Geophysics* 81 (1), G13–G26.
- Wu, L., Lin, Q. 2017. Improved Parker’s method for topographic models using Chebyshev series and low rank approximation. *Geophysical Journal International* 209 (2), 1296–1325.
- Yano, H., Kubota, T., Miyamoto, H., Okada, T., Scheeres, D., Takagi, Y., Yoshida, K., Abe, M. 2006. Touchdown of the Hayabusa spacecraft at the muses sea on Itokawa. *Science* 312 (5778), 1350–1353.
- Yeomans, D. K. 1995. Asteroid 433 Eros: the target body of the NEAR mission. *Journal of the Astronautical Sciences* 43 (4), 417–426.